Chemical Physics Letters 842 (2024) 141212

Contents lists available at ScienceDirect

Chemical Physics Letters

journal homepage: www.elsevier.com/locate/cplett

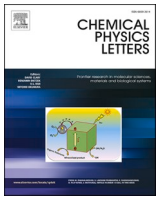

Unraveling the ignition chemistry of singly levitated aluminum iodate hexahydrate (AIH) particles

Grace L. Rizzo [a], Souvick Biswas [a], Michelle L. Pantoya [b,*], Ralf I. Kaiser [a,*]

[a] Department of Chemistry, University of Hawai'i at Manoa, Honolulu, HI 96822, USA
[b] Department of Mechanical Engineering, Texas Tech University, Lubbock, TX 79409-1021, USA

A B S T R A C T

The ignition chemistry of a newly synthesized oxidizing salt, aluminum iodate hexahydrate ($[Al(H_2O)_6](IO_3)_3(HIO_3)_2$; AIH), while acoustically levitated in the presence of molecular oxygen inside a controlled process chamber is reported. Exploiting temporally resolved ultraviolet–visible (UV–Vis) spectroscopy, a complex pool of reactive transients has been detected, namely- aluminum monoxide (AlO), atomic aluminum (Al), atomic iodine (I), iodine monoxide (IO), atomic oxygen (O), along with stable products such as molecular iodine (I_2) and water (H_2O). The plausible pathways for the ignition process have been proposed which reveal AIH as a potential additive in hydrocarbon-based and solid rocket fuels in the near future.

1. Introduction

Since the very first incorporation of the internal combustion engine in a motor vehicle by Carl Benz in 1886 [1], hydrocarbon-based fuels have been exploited for nearly 150 years as an energy source for automobiles, airplanes, and rocket propulsion systems [2]. Although hydrocarbon-based fuels such as *exo*-tetrahydrodicyclopentadiene (JP-10, $C_{10}H_{16}$) for jet engines represent the most widely consumed energy source, the limited volumetric energy density of traditional hydrocarbon fuels of up to 40 kJ cm^{-3} motivated the materials scientific community to develop advanced fuels with higher performance, efficiency, and energy densities [3,4]. Metal-doped nanomaterials such as aluminum nanoparticles have emerged as a promising additive to hydrocarbon fuels with aluminum nanoenergetic materials (ALNEM) chosen for their high energy density (84 kJ cm^{-3}) and affordability [5–7]. However, the aluminum oxide (Al_2O_3) passivation layer of these ALNEMs acts as a heat sink and restrains the diffusion of oxygen to the aluminum metal core thereby decreasing the reactivity of the aluminum core [8–10]. To combat this, aluminum iodate hexahydrate ($[Al(H_2O)_6](IO_3)_3(HIO_3)_2$; AIH) has materialized as a substitute for the native oxide layer to enhance the reactivity of ALNEMs [11–13]. The molecular structure of AIH (Fig. 1)[14] not only offers passivation protection of the Al core particle [11], but also an abundance of additional oxidizing species to support oxidation reactions with the Al core [12]. Benchmark studies of aluminum thermites containing both ALNEMs and AIH showed dramatic increases in flame speed as high as 3200 ms^{-1} [12,15], whereas thermites without AIH only demonstrated flame speeds of 682 ms^{-1} [9].

However, the addition of AIH to nano metal-doped hydrocarbon fuels and the de-facto replacement of the passivation layer in actual jet engines requires new knowledge of the decomposition mechanisms and inherent chemistry of AIH on the molecular level ultimately leading to enhanced engine performance [16,17]. Thermal stability studies under equilibrium conditions revealed that AIH decomposes in three distinct stages [17]. However, an understanding of the effect of oxygen on the thermal decomposition and even oxidation of AIH itself is in its infancy.

The objective of this study is to investigate the exothermic decomposition and reaction of singly levitated AIH particles to resolve the chemical kinetics and provide an inventory of open and closed shell species in AIH oxidation. Individual AIH particles are levitated within an ultrasonic levitator. This unit is encapsulated in a stainless-steel process chamber filled with an oxygen-argon atmosphere at distinct concentrations of oxygen in argon starting from 10 % to 80 % oxygen. Exploiting time-resolved ultraviolet–visible (UV–Vis) emission spectroscopy, this study reveals the existence of, e.g., various oxygen-centered radical transients along with closed shell species initiating a complex chain of reactions during the ignition of AIH: aluminum (Al), hydroxyl radical (OH), aluminum monoxide (AlO), iodine monoxide (IO), molecular iodine (I_2), iodine (I), oxygen (O), and water (H_2O). These assignments were cross-checked and confirmed through ignition experiments with partially deuterated aluminum iodate hexahydrate ($[Al(D_2O)_6]$ $(IO_3)_3(HIO_3)_2$; AID). These studies afforded an understanding of the gas-phase oxidation of AIH in nanometal-doped hydrocarbon fuels like JP-10 along with likely reaction mechanisms involving a previously undocumented pool of reactive radical species ultimately

* Corresponding authors.
E-mail addresses: michelle.pantoya@ttu.edu (M.L. Pantoya), ralfk@hawaii.edu (R.I. Kaiser).

https://doi.org/10.1016/j.cplett.2024.141212
Received 12 January 2024; Received in revised form 14 March 2024; Accepted 17 March 2024
Available online 20 March 2024

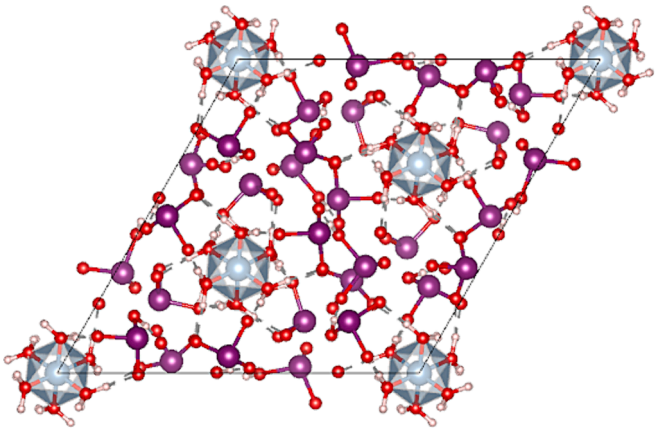

Fig. 1. Graphical representation of the crystal structure of aluminum iodate hexahydrate (AIH). Grey spheres represent Al, red spheres represent O, white spheres represent H, and purple spheres represent I [14]. (For interpretation of the references to colour in this figure legend, the reader is referred to the web version of this article.)

aiding the development of next generation additives for hydrocarbon and solid rocket fuels.

2. Methods

2.1. Materials

Aluminum iodate hexahydrate ($[Al(H_2O)_6](IO_3)_3(HIO_3)_2$; AIH) and partially deuterated aluminum iodate hexahydrate ($[Al(D_2O)_6](IO_3)_3(HIO_3)_2$; AID) particles were synthesized in house as described in detail by Miller et al [17]. Briefly, particles were prepared exploiting an acid-base precipitation reaction that can be summarized in three steps. Synthesis began by dissolving iodine pentoxide (I_2O_5) powder (Sigma Aldrich) in water - either H_2O or D_2O - at a 1:1 wt ratio. Following preparation of this highly acidic solution, aluminum hydroxide ($Al(OH)_3$) powder (Sigma Aldrich) was introduced and heated mildly (363 K) to facilitate dissolution. For large crystal formation, the solution was removed from heat and slowly evaporated under ambient conditions precipitating the formation of mm-scale particles [17]. This procedure was optimized to yield particle sizes of typically 1 mm considering that the largest particles that could be steadily levitated were about 2.5 mm in size. Argon (99.9999 %, Ar) and oxygen (99.999 %, O_2) were obtained from Airgas.

2.2. Ultrasonic levitator apparatus

The experiments were carried out utilizing an ultrasonic acoustic levitator [18–20]. Ultrasonic sound waves were generated from a piezoelectric transducer oscillating at 58 kHz (Figure S1). A standing wave is generated through multiple reflections between the transducer (bottom) and concave reflector (top). The distance between the transducer and reflector is adjusted by a micrometer manipulator to an integral number of half wavelengths which allows for resonance conditions to be maintained following any changes that occur in gas composition, temperature, or pressure. A typical distance between the front plate and reflector is selected to 2.5 times the wavelength (14.8 mm) resulting in five pressure nodes. The amplitude of the oscillations can be optimized through an adjustment of the radio frequency (RF) power between 0.7 and 5.0 W and monitoring the feedback voltage on an oscilloscope. The levitator is housed within a pressure compatible stainless-steel process chamber (Fig. 2) [16]. This enables the AIH and AID particles to be studied in a well-defined and contained oxygen-argon environment at elevated pressures. To stabilize the particles in the third pressure node of the standing wave, experiments were carried out at a pressure of 1200 Torr, measured by a MKS 626B Baratron.

2.3. Solid particle sampling

Solid samples are levitated slightly below the pressure minima of the ultrasonic standing wave [16,18,19]. This is feasible since the acoustic

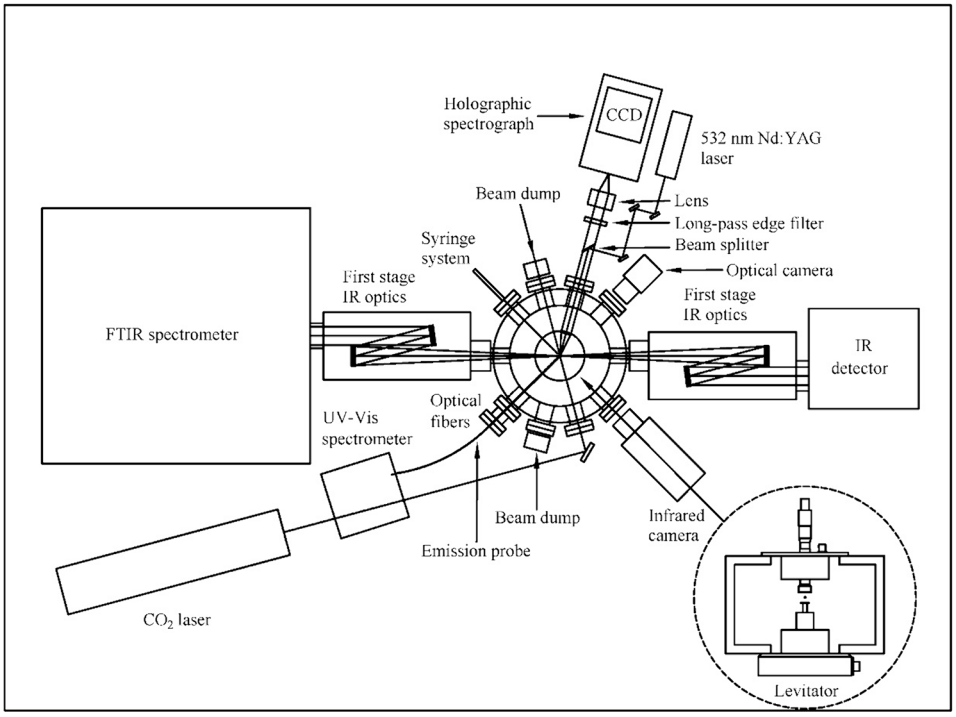

Fig. 2. Schematic top view of the complete levitator apparatus displaying the ultrasonic levitator, process chamber, carbon dioxide laser, Raman spectrometer, infrared camera, optical camera, and some other complementary spectroscopy tools (FTIR spectrometer and fiber optic UV–vis spectrometer) [16].

radiation pressure from the sound waves counteracts the gravitational force. The horizontal restoring force centers the particle on the axis of the levitator. In the single axis levitator, this horizontal force is one order of magnitude smaller than the axial force. The particles are introduced to the central pressure node via a magnetically coupled wobble stick attached to a side port of the process chamber. The 1 cm × 1 cm stainless-steel wire mesh is attached to the end of the wobble stick shaping an acoustically transparent spatula inside of the process chamber, which holds the AIH or AID sample [16,18,19].

2.4. Heating of particles

To initiate heating and eventually ignition of the levitated particle, a 40 W carbon dioxide (CO_2) laser emitting at 10.6 μm (Synrad, Inc., model FSV40KFD) was used [16,18,19]. The output power of the laser was externally triggered and synchronized using a pulse delay generator (Quantum Composers, 9518 plus). The CO_2 laser was operated in burst mode with a delay of 100 ms (Fig. 3). The overall duty cycle used in the experiments was 80 % with a repetition rate of 1 kHz. This output of the laser passes a zinc selenide window and was introduced to the center of the levitator by a parabolic copper mirror. The diameter of the laser beam was focused to a diameter of 0.2 mm onto the particle. This was achieved by using an eight-fold beam expander followed by a parabolic copper mirror with a focal length of 300 mm. The exiting beam from the laser had a diameter of 2.5 mm with a beam divergence angle of less than 7.0 mR [16].

Additionally, the CO_2 laser is utilized to mimic the operational temperature of the combustion engines. The heating of the laser represents real life applications of extreme heating of fuel caused by a fuel igniter in a combustion engine. This allows us to systematically study the effect of temperature and assess the physical and chemical changes which are essential to decipher the complexity in common combustion reactions. The characterization of how the heat from the CO_2 laser is propagated throughout the levitated samples to ignite the samples has been discussed in previous studies [18,19,21].

2.5. Ultraviolet–visible spectrometer

The ultraviolet–visible (UV–Vis) spectra were collected in situ in the wavelength region of 200 to 1,100 nm using a StellarNet SILVER-Nova zAP1 UV–Vis spectrometer with a fiber optic probe (high OH fused silica core; 200–1100 nm) [22]. The end of the fiber optic probe is attached to an x, y, z manipulator to position the receiving end of the probe at an optimal distance from the ignition. In this experiment, the end of the probe was positioned at 13 mm from the center of the levitator. For every measurement, the UV–Vis spectrometer operated at 1 kHz rate, collecting 127 consecutive spectra. The detector integration time was set to 6 ms. The UV–Vis spectrometer was externally triggered and synchronized to the CO_2 laser with a delay of 100 ms. The wavelength-dependent sensitivity calibration for the spectrometer system, including the optical fiber has been performed prior to experimental run and the methods are briefly outlined in the Supporting Information.

2.6. Optical and infrared videos

To capture the ignition event of the AIH and AID particles, a Phantom Miro 3a10 camera operating at 1 kHz was used. This is equipped with a Navitar Zoom 6000 modular lens system. Infrared thermal imaging videos were collected in tandem with the optical videos using a FLIR A6703sc IR camera. An ND2 filter was used to attenuate the intensity while working in the high temperature range (523 K-1,773 K). The infrared (IR) camera was set to a repetition rate of 250 Hz. Both cameras were externally triggered by the pulse delay generator without any delay referenced to the trigger pulse.

3. Results

3.1. Optical and IR images

High-speed optical and infrared images were captured to visualize the ignition process of the particles and track the associated temperature changes, respectively. Optical and IR videos are deposited in the Supporting Information (Movies M1-M8 and M1IR-M8IR). Extracted snapshots of the ignitions are displayed in Fig. 4 for individual AIH particles levitated in 20 % O_2 and 80 % O_2, where 20 % O_2 mimics the atmospheric oxygen content and intake in a combustion engine. Snapshots for the remaining concentrations are compiled in Figures S2-S7.

With the start of the ignition in 20 % O_2 (Fig. 4a), the temperature rapidly reached 1,402 K after 156 ms (Fig. 4b). At this stage, a weakly colored orange cloud formed around the particle. As the temperature rose to 1,947 K, a rapid increase in the size of the particle by a factor of two in volume was noted. During the first phase of the thermal AIH decomposition in the absence of oxygen at 375 K, a loss of water followed by a volume increase by nearly 200 % of its original volume was detected [16]. In the present case, the rapidly increasing temperature to nearly 2,000 K could release crystal water and also evaporate water thus leading to the observed volume expansion of the levitated particle. In the second stage of the ignition process, the flame brightens, and a white glow emerges. This white glow is enhanced with increasing the molecular oxygen concentration and becomes most prominent at 80 % O_2

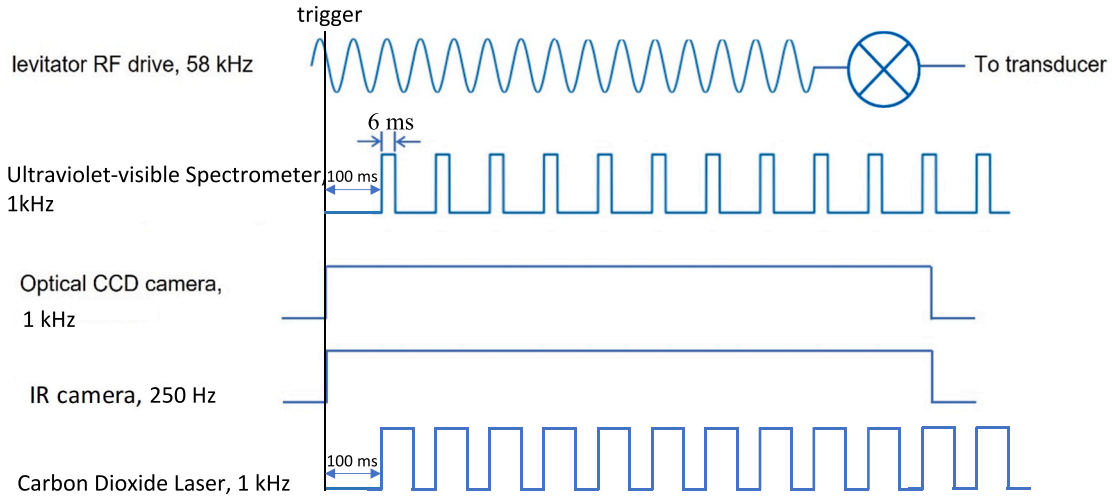

Fig. 3. Typical pulse sequence used for operation of the ultrasonic levitator coupled with time resolved emission spectroscopy and imaging tools.

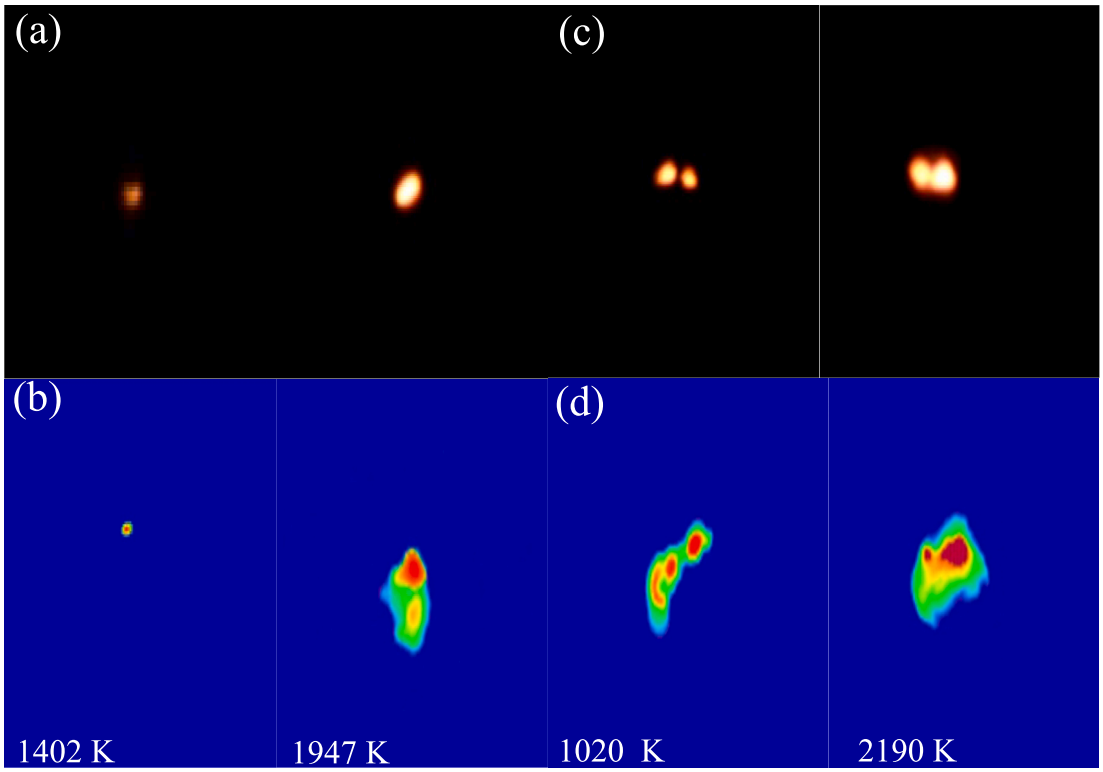

Fig. 4. Optical and IR camera images taken during the ignition of AIH. (a) represents the optical images taken during ignition in 20% O_2 and 80% Ar. The image on the left is at the beginning of the ignition and the right is the point of the ignition where it is most intense. (b) represents the respective IR camera images to the images shown in (a). The respective temperatures are shown at the bottom of (b). (c) represents the optical images taken during ignition in 80% O_2 and 20% Ar. The image on the left is at the beginning of the ignition and the right is the point of the ignition where it is most intense. (d) represents the respective IR camera images to the images shown in (c). The respective temperatures are shown at the bottom of (d).

(Fig. 4c,d); this enhancement also correlates with the rise in maximum temperature to 2,190 K (Table 1). Overall, peak temperatures did not exceed 2,200 K and essentially increased slightly from 1,882 K (10 % O_2) to 2,190 K (80 % O_2).

3.2. *Uv–vis emission spectroscopy*

UV–vis emission profiles represent an excellent diagnostic tool for the detection of gas-phase species formed during the oxidation process. A characteristic set of emission spectra acquired for the ignition of the AIH particle in 20 % O_2 medium is displayed in Fig. 5; the UV–vis sets for the remaining oxygen concentrations can be found in Figures S8-S14.

For 20 % O_2, the ignition started 156 ms after the first pulse from the CO_2 laser; the burn time lasted for 126 ms with the most intense emissions observed at 270 ms in the late oxidation phase. This finding is consistent with images of the optical camera (Movies M2 and M2IR). Both the UV–vis and optical videos also agree that the oxidation process is not continuous; as a result, some of the UV–vis emission spectra did not contain any discernible spectral features. Overall, the emission spectra reveal pronounced black body radiation profiles along with overlaid individual emission peaks. A comprehensive identification of open- and closed-shell species formed during the oxidation of AIH was achieved by analyzing the time-resolved UV–vis spectra. Electronic transitions are assigned from the blackbody-corrected deconvoluted spectral traces for each concentration of oxygen as displayed in Fig. 6 (20 % O_2) and Figures S15-S21. The resulting peak assignments have been compiled in Tables 2 and S1-S7 [22–24]. For selected molecular species with well-known molecular spectrum namely aluminum monoxide (AlO B-X, C-X, D-X), iodine monoxide (IO A-X) and molecular iodine (I_2 B-X), PGOPHER simulations (Supporting information) [24] were used to determine the line centers of major spectral bands [22]. At all oxygen concentrations, atoms, radicals and molecules were observed and serve as the key transients for the complex series of reactions during AIH oxidation.

Table 1
Summary of all maximum temperatures reached for AIH levitated in each % of O_2.

% of O_2	Temperature (K) ± 40 K
10	1,882
20	1,947
30	2,151
40	2,141
50	2,153
60	2,082
70	2,135
80	2,190

Atoms (Al, I, O): Several atomic emissions were observed in the emission spectrum of AIH in 20 % O_2 (Fig. 6). The most important emissions originate from atomic aluminum (Al; ^{2}P) and iodine (I; ^{2}P) transitions. Aluminum, an obvious intermediate identified in previous combustion studies utilizing ALNEMs [7,22], is associated with the 4s ^{2}S – 3p $^2P^o$ transition at 392.9 nm; the most dominant peak for atomic iodine in the 20 % O_2 spectrum is associated with the 6s ^{2}[2] – 5p^5 $^2P^o$ transition at 207.9 nm. In addition to these atomic emissions, atomic oxygen (O; ^{3}P) was also identified at all concentrations and can be linked to the 4d $^5D^o$ – 3p ^{5}P transition at 616.2 nm. Apart from the aforementioned emissions, Na (3p $^2P^o$ – 3s ^{2}S, 586.7 nm), K (5p $^2P^o$ – 4s ^{2}S, 405.8 nm), and Li (2p $^2P^o$ – 2s ^{2}S, 674.2 nm) are identified in the emission spectra as impurities during the ignition of aluminum-based particles [7,22].

Diatomic Radicals (AlO, IO, OH): The most prominent emission features are associated with the open shell species aluminum monoxide

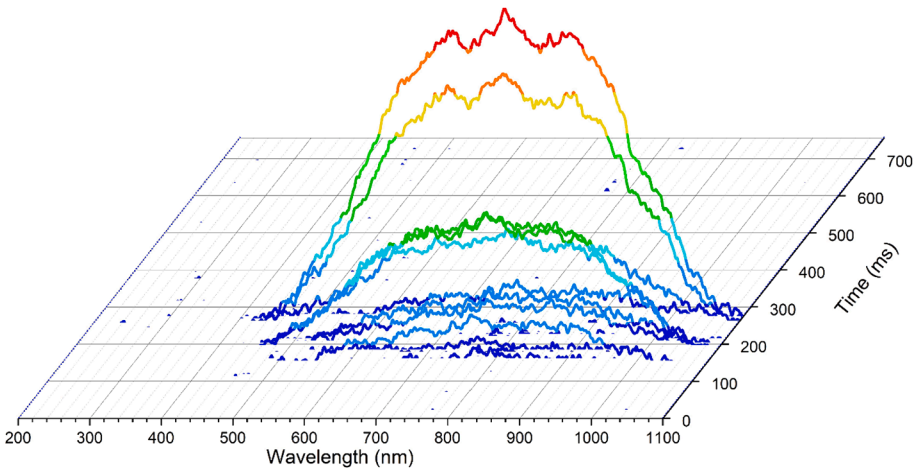

Fig. 5. 3D plot of the AlH emission spectra when levitated in 20% O_2 and 80% Ar.

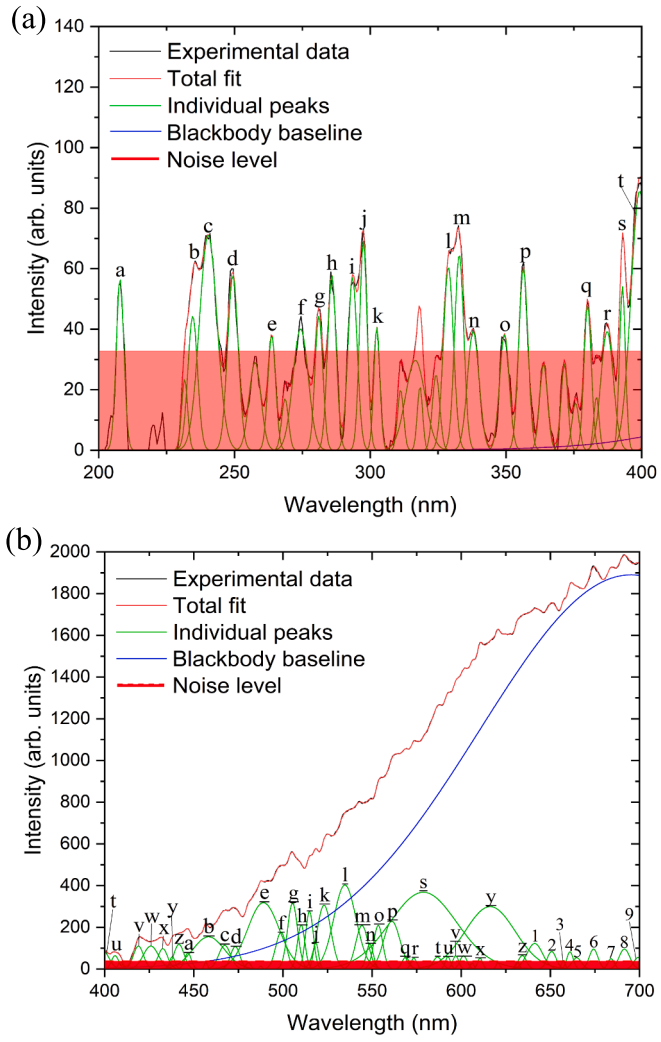

Fig. 6. Deconvoluted UV–Vis emission spectrum of the levitated AlH particle during ignition in 20 % O_2 and 80 % Ar. (a) represents the wavelength region from 200 to 400 nm and (b) represents the wavelength region from 400 to 700 nm. See Table 2 for peak assignments.

(AlO; $X^2\Sigma^+$) and iodine monoxide (IO; $X^2\Pi_{3/2}$). The strongest AlO peaks are linked to the $B^2\Sigma^+ - X^2\Sigma^+$ transition between 438 and 597 nm with the strongest peak at 534.8 nm. In the UV segment, some weaker AlO transitions are also present in the 20 % O_2 emission spectrum. These bands are associated with the $D^2\Sigma^+ - X^2\Sigma^+$ and $C^2\Pi - X^2\Sigma^+$ transitions within the range of 234–281 nm and 293–338 nm with strongest peaks at 249.4 nm and 332.8 nm, respectively. The IO emissions are associated with the $A^2\Pi_{3/2} - X\ ^2\Pi_{3/2}$ transition found at 441.7 nm and 548.7 nm with the strongest of these two peaks located at 441.7 nm. These peaks have been found to be associated with the excited state level $\nu = 2$. The other excited state levels ($\nu = 0$, 1, 3) are found to be strongly predissociative and therefore cannot be detected in the timescale of these experiments [25,26]. The remaining weak features consist of the hydroxyl radial (OH; $X\ ^2\Pi$). The OH transition ($A^2\Sigma^+ - X^2\Pi$) is weak (285.9 nm) and was found only at 20 %, 30 %, and 40 % O_2 concentration.

Closed Shell Molecules (I_2, H_2O): Lastly, two closed shell species have been identified as present in the emission spectrum. These species include molecular iodine (I_2; $X\ ^1\Sigma_g^+$) and water (H_2O, X^1A_1). The molecular iodine (I_2) emissions are associated with the $B^3\Pi_{0+u} - X^1\Sigma_g^+$ transition between 510 nm and 665 nm with the strongest peak at 578.8 nm. These features and those linked to IO and AlO have been found to be the most dominant emissions for all oxygen concentrations. Finally, a weak emission feature of H_2O is detected in all concentrations except 10 % O_2; it can be linked with the segments of ro-vibronic transitions at 674–699 nm. The strongest of these peaks is detected at 691.6 nm. It is worth mentioning that minor species are tentatively assigned due to spectral overlapping. Table S8 lists the number of peaks that show up as unique assignments for individual species. Amongst all detections, the species with the most unique peaks and no overlapping emissions are AlO (D-X, C-X, B-X), IO, I_2, H_2O, Na, and Li. The species with the least number of unique peaks are associated with I, Al, OH, O, and K.

Emission Profiles: Utilizing the emission spectra, the temporal evolution of selected species can be obtained (Figures S22-S29). At all oxygen concentrations, these graphs do not display smooth curves; instead, sudden spikes in intensity and drops to little to no intensity are evident. These patterns can be attributed to non-continuous oxidation processes causing uneven heating of the particles and intensity in the glow during the oxidation.

Temperature Profiles: Exploiting the temperatures captured by the IR camera, the temperature profiles were plotted to visualize the temperature changes over time. The IR camera underestimates the flame temperature by a factor of 2 to 3 [7,22] because the temperature measured by the IR camera is proportional to the flame emissivity ε. To correct this, the temperatures obtained from the blackbody emission curves were used as calibration. The temperature extraction from the UV–Vis spectra was performed utilizing a Python code [22]. The sensitivity of the UV–Vis spectrometer and fiber optic probe (Figure S30b) combined is used to correct the measured spectra prior to further analysis and temperature fittings. This is performed within the Python

Table 2
Peak assignments for the deconvoluted emission spectrum of AlH particle levitated in 20% O_2 and 80% Ar.

Peak/band	Peak wavelength/band center (nm)	Carrier	Reference wavelength (nm)[a,b,c]	Transition	Branch; spin–orbit components; vibrational quantum numbers: (ν', ν'') or ($\nu1'$,$\nu2'$,$\nu3'$) – ($\nu1''$,$\nu2''$,$\nu3''$)
a	207.9	I	206	$6s\ ^2[2] - 5p^5\ ^2P^o$	3/2 – 1/2
b	234.6	AlO	235	$D\ ^2\Sigma^+ - X\ ^2\Sigma^+$	(3,0)
c	240.3	Li	242	$7p\ ^2P^o - 2s\ ^2S$	3/2 – 1/2; 1/2 – 1/2
		AlO	239	$D\ ^2\Sigma^+ - X\ ^2\Sigma^+$	(2,0)
d	249.4	AlO	249	$D\ ^2\Sigma^+ - X\ ^2\Sigma^+$	(0,0)
e	263.7	AlO	262	$D\ ^2\Sigma^+ - X\ ^2\Sigma^+$	(0,2)
f	274.4	Li	274	$4p\ ^2P^o - 2s\ ^2S$	1/2 – 1/2; 3/2 – 1/2
		Al	274	$4d\ ^2F^o - 4d\ ^2D$	7/2 – 5/2; 5/2 – 3/2
		AlO	275	$D\ ^2\Sigma^+ - X\ ^2\Sigma^+$	(1,5)
g	281.1	AlO	282	$D\ ^2\Sigma^+ - X\ ^2\Sigma^+$	(0,5)
h	285.9	OH	287 – 289	$A\ ^2\Sigma^+ - X\ ^2\Pi$	R_1, R_2, Q_1, Q_2; (2, 1)
		Na	285	$5p\ ^2P^o - 3s\ ^2S$	3/2 – 1/2; 1/2 – 1/2
i	293.5	Al	291	$4d\ ^2D^o - 4d\ ^2D$	5/2 – 5/2; 3/2 – 3/2
		AlO	289	$C\ ^2\Pi - X\ ^2\Sigma^+$	(3,1)
j	297.5	AlO	296	$C\ ^2\Pi - X\ ^2\Sigma^+$	(1,0)
		O	297	$2p^4\ ^1S - 2p^4\ ^3P$	0 – 1
k	302.4	AlO	303	$C\ ^2\Pi - X\ ^2\Sigma^+$	(0,0)
l	328.8	Na	330	$4p\ ^2P^o - 3s\ ^2S$	3/2 – 1/2; 1/2 – 1/2
m	332.8	AlO	332	$C\ ^2\Pi - X\ ^2\Sigma^+$	(2,5)
n	337.9	AlO	340	$C\ ^2\Pi - X\ ^2\Sigma^+$	(0,4)
o	349.4	Na	348	$3d\ ^4D^o - 3p(^3P^o)\ ^4S$	5/2 – 3/2
p	356.4	Na	350	$3d\ ^4P^o - 3p(^3P^o)\ ^4S$	3/2 – 3/2
		Na	351	$3d\ ^4P^o - 3p(^3P^o)\ ^4S$	1/2 – 3/2
q	380.1	Li	379	$7d\ ^2D - 2p\ ^2P^o$	3/2 – 1/2; 5/2 – 3/2; 3/2 – 3/2
r	387.3	Na	388	$3d\ ^4F^o - 3p(^3P^o)\ ^4D$	9/2 – 7/2;
				$4s\ ^2S - 3s\ ^2S$	1/2 – 1/2;
				$3d\ ^4D^o - 3p(^3P^o)\ ^4D$	3/2 – 3/2
s	392.9	Li	391	$6d\ ^2D - 2p\ ^2P^o$	3/2 – 1/2; 5/2 – 3/2; 3/2 – 3/2
		Na	391	$3d\ ^4F^o - 3p(^3P^o)\ ^4D$	7/2 – 5/2
		Al	394	$4s\ ^2S - 3p\ ^2P^o$	1/2 – 1/2
		O	394	$4p\ ^5P - 3s\ ^5S^o$	3–2; 2–2; 1–2
t	399.3	Na	399	$3d\ ^4P^o - 3p(^3P^o)\ ^4D$	3/2 – 3/2
		Na	400	$3d\ ^4P^o - 3p(^3P^o)\ ^4D$	1/2 – 3/2
		Al	396	$4s\ ^2S - 3p\ ^2P^o$	1/2 – 3/2
u	405.8	K	404	$5p\ ^2P^o - 4s\ ^2S$	3/2 – 1/2; 1/2 – 1/2
v	419.0	Na	418	$3d\ ^4D^o - 3p(^3P^o)\ ^4P$	5/2 – 5/2
w	425.9	Na	425	$3d\ ^4D^o - 3p(^3P^o)\ ^4P$	5/2 – 3/2
		Al	425	$3d\ ^2D^o - 5d\ ^2D$	5/2 – 5/2
x	432.6	Na	432	$9d\ ^2D - 3p\ ^2P^o$	3/2 – 1/2; 3/2 – 3/2; 5/2 – 3/2
y	438.0	AlO	436	$B\ ^2\Sigma^+ - X\ ^2\Sigma^+$	(5,2)
z	441.7	IO	440	$A\ ^2\Pi_{3/2} - X\ ^2\Pi_{3/2}$	(2,1)
a	446.7	Na	443	$4s\ ^4P^o - 3p(^3P^o)\ ^4S$	5/2 – 3/2
b	458.3	Li	460	$4d\ ^2D - 2p\ ^2P^o$	3/2 – 1/2; 5/2 – 3/2; 3/2 – 3/2
c	467.3	AlO	467	$B\ ^2\Sigma^+ - X\ ^2\Sigma^+$	(1,0)
d	473.2	K	474	$13s\ ^2S - 4p\ ^2P^o$;	1/2 – 1/2; 3/2 – 1/2
				$11d\ ^2D - 4p\ ^2P^o$	
e	489.1	I	491	$7p\ ^2[2]^o - 6s\ ^2[2]$	5/2 – 5/2
f	498.9	K	496	$8d\ ^2D - 4p\ ^2P^o$	5/2 – 3/2
g	505.4	Na	507	$4s\ ^4P^o - 3p(^3P^o)\ ^4D$	7/2 – 5/2
h	510.2	I_2	509	$B\ ^3\Pi_{0+u} - X\ ^1\Sigma_g^+$	(46,0)
i	514.9	AlO	510	$B\ ^2\Sigma^+ - X\ ^2\Sigma^+$	(0,1)
		I	511	$7p\ ^2[1]^o - 6s\ ^2[2]$	3/2 – 3/2
j	518.4	Na	516	$4s\ ^4P^o - 3p(^3P^o)\ ^4D$	5/2 – 5/2
k	523.1	I	523	$7p\ ^2[3]^o - 6s\ ^2[2]$	5/2 – 3/2
l	534.8	AlO	538	$B\ ^2\Sigma^+ - X\ ^2\Sigma^+$	(1,3)
m	544.3	I	542	$6p\ ^2[1]^o - 6s\ ^2[2]$	3/2 – 5/2
		I_2	545	$B\ ^3\Pi_{0+u} - X\ ^1\Sigma_g^+$	(25,0)
n	548.7	IO	550	$A\ ^2\Pi_{3/2} - X\ ^2\Pi_{3/2}$	(2,5)
o	553.4	Na	556	$4s\ ^4P^o - 3p(^3P^o)\ ^4P$	3/2 – 3/2
		Al	555	$6p\ ^2P^o - 4s\ ^2S$	3/2 – 1/2; 1/2 – 1/2
p	561.1	O	557	$2p^4\ ^1S - 2p^4\ ^1D$	0–2
q	568.8	AlO	565	$B\ ^2\Sigma^+ - X\ ^2\Sigma^+$	(2,5)
r	573.4	I_2	574	$B\ ^3\Pi_{0+u} - X\ ^1\Sigma_g^+$	(17,1)
s	578.8	I_2	578	$B\ ^3\Pi_{0+u} - X\ ^1\Sigma_g^+$	(16,1)
t	586.7	I_2	585	$B\ ^3\Pi_{0+u} - X\ ^1\Sigma_g^+$	(16,2)
		Na	588	$3p\ ^2P^o - 3s\ ^2S$	3/2 – 1/2
u	592.5	I_2	592	$B\ ^3\Pi_{0+u} - X\ ^1\Sigma_g^+$	(14,2)
		Na	589	$3p\ ^2P^o - 3s\ ^2S$	1/2 – 1/2

(*continued on next page*)

Table 2 (*continued*)

Peak/band	Peak wavelength/band center (nm)	Carrier	Reference wavelength (nm)[a,b,c]	Transition	Branch; spin–orbit components; vibrational quantum numbers: (ν', ν'') or ($\nu1'$,$\nu2'$,$\nu3'$) – ($\nu1''$,$\nu2''$,$\nu3''$)
v	596.9	I_2	596	B $^3\Pi_{0+u}$ – X $^1\Sigma_g^+$	(13,2)
		AlO	595	B $^2\Sigma^+$– X $^2\Sigma^+$	(2,6)
w	601.3	I_2	600	B $^3\Pi_{0+u}$ – X $^1\Sigma_g^+$	(12,2)
x	610.6	I_2	611	B $^3\Pi_{0+u}$ – X $^1\Sigma_g^+$	(11,3)
		Li	610	3d ^{2}D – 2p ^{2}P^o	3/2 – 1/2; 5/2 – 3/2; 3/2 – 3/2
y	616.2	O	615	4d ^{5}D^o – 3p ^{5}P	1–1; 3–2; 4–3
z	634.3	I_2	636	B $^3\Pi_{0+u}$ – X $^1\Sigma_g^+$	(7,4)
1	641.2	I_2	641	B $^3\Pi_{0+u}$ – X $^1\Sigma_g^+$	(8,5)
		O	645	5s ^{5}S^o – 3p ^{5}P	2–1; 2–2; 2–3
2	650.8	I_2	649	B $^3\Pi_{0+u}$ – X $^1\Sigma_g^+$	(8,6)
3	657.3	I_2	654	B $^3\Pi_{0+u}$ – X $^1\Sigma_g^+$	(7,6)
4	661.0	O	660	5s ^{1}D^o – 3p ^{1}F	2–3
5	664.8	I_2	664	B $^3\Pi_{0+u}$ – X $^1\Sigma_g^+$	(5,6)
6	674.2	H_2O	632–683	ro-vib. mode	(1,1,3) – (1,5,1)
		Li	670	2p ^{2}P^o – 2s ^{2}S	3/2 – 1/2; 1/2 – 1/2
7	684.0	H_2O	632–683	ro-vib. mode	(1,1,3) – (1,5,1)
8	691.6	H_2O	690–710	ro-vib. mode	(1,0,3) – (0,0,0)
		K	693	4d ^{2}D – 4p ^{2}P^o; 6s ^{2}S – 4p ^{2}P^o	3/2 – 1/2; 1/2 – 3/2
9	699.4	H_2O	690–710	ro-vib. mode	(1,0,3) – (0,0,0)

[a] Ref. [22].
[b] Ref. [23].
[c] Ref. [24].

code by taking the raw data and dividing by the sensitivity curve; the resultant spectrum is then fitted with Planck's blackbody radiation formula [22] to obtain the temperatures. There were points in the UV–Vis spectra where no emission was detected during ignition; those can be correlated with the dark time in the optical camera videos. However, the IR camera detected that even though no emission peaks were evident, the particles were still hot. The resulting temperature profiles are displayed in Figure S31. For 20 % O_2, temperature spikes emerged reaching up to 1,402 K once particles ignite at 156 ms. Followed by a burn phase, a maximum temperature of 1,947 K was reached. In general, across all concentrations, the temperature profiles reveal AIH burn time exceeding 100 ms.

3.3. AID ignition

Optical and IR videos for AID particle oxidation can be found in the Supporting information (Movies M9 and M9IR). Comparing the ignition and temperature profiles of AIH in 20 % O_2 with the AID in 20 % O_2, there is no significant change between the two particles. AID (Figure S32) in 20 % O_2 revealed a temperature of 1,675 K at the beginning of the oxidation reaching a maximum temperature of 1,970 K. This peak temperature can then be compared to the maximum temperature (1,947 K) of AIH in 20 % O_2 (Fig. 4b). This comparison manifests that both temperatures are within the error limit. Additional data indicating no discernible distinction between the AIH and AID ignitions are found in both the temporal evolution (Figure S33) and temperature (Figure S34) profiles. The temperature profile does, however, demonstrate that AID had a smoother ignition as less sudden spikes in temperature are seen in AID detected in the temperature profile of AIH in 20 % O_2 (Figure S31). For AID, the particles ignite at 192 ms reaching the initial temperature of 1,675 K. The burn time lasted for 174 ms with the maximum temperature of 1,947 K being detected. Similarly, in the emission spectral series during ignition, AID (Figure S35) had notable similarities to AIH with similar ignition delays and durations. The AID was fully ignited at 192 ms since the exposure to the laser and the ignition survived 174 ms with the most intense emissions at 336 ms. AID having a long burn time of more than 100 ms (174 ms) indicates that AID has an extended ignition as previously noted in AIH particles. When comparing the deconvoluted spectra of AIH and AID in 20 % O_2 (Fig. 6 and Figure S36), all species identified reveal an identical inventory. However, one distinct and key difference is the detection of deuterated hydroxyl radical (OD; X $^2\Pi$). These peaks are associated with the A $^2\Sigma^+$–X $^2\Pi$ transition at 264.3, 289.7, and 294.6 nm (Table S9) [22–24,27]. Two out of the three OD peaks can be identified as unique assignments with no overlapping in assignments. Therefore, isotopic substitution experiments such as provided here can be exploited to cross-check assignments of the UV–vis emission spectra.

4. Discussion

The captured images revealed two stages of AIH oxidation. The initial phase of the oxidation is characterized by a weakly colored orange cloud formed around the particle. In the second stage of the oxidation, the flame brightens, and a white glow is observed. This increase in brightness and glow represents an increase in emission intensity which correlates with the number densities of the emitting species. The second stage is connected with an enhanced oxidative decomposition of the AIH particles as the white glow is increasing with rising percentage of molecular oxygen. As a matter of fact, the detected number of emission peaks also increases along with the gain in intensity. The oxidation is facilitated when we move from 10 % to 20 % molecular oxygen (Figures S15 and 6) exhibiting an increase in AlO and IO peaks. The extended oxidation in the second stage (Fig. S2a-S7a and Fig. 4a,c) could also originate from the gaseous molecular oxygen released from the particle itself through the decomposition of I_2O_5, which facilitates in situ oxidation reactions leading to combustion of the particles [16].

The aforementioned results derived from the emission traces and visual images imply a complex chemistry involving both aluminum (Al) and iodine (I) driving the oxidation. In this section, an attempt has been made to disentangle the reactions and ultimately propose a plausible mechanistic picture. At all oxygen concentrations, key atomic, radical, and closed-shell species were observed. The atomic species identified include atomic aluminum (Al), iodine (I), and oxygen (O). The diatomic radicals observed in the emission spectra include aluminum monoxide (AlO), iodine monoxide (IO), and the hydroxyl radical (OH) with the latter verified explicitly through the detection of the D1-hydroxyl

radical (OD). Finally, two closed-shell molecules detected were iodine (I_2) and water (H_2O). To understand how these species are formed during oxidation, the primary steps of the AIH thermal decomposition can be recalled from previous studies [16]. The first step is associated with the water loss at 375 K followed by a conversion of iodic acid (HIO_3) into diiodine pentoxide (I_2O_5) and water (H_2O) at 480 K. In the third step, a rapid decomposition of diiodine pentoxide into the gaseous elements, iodine (I_2) and oxygen (O_2), at 580 K has been seen. With further rise in temperature (800 K), it was revealed that aluminum iodate ($Al(IO_3)_3$) disintegrates to form aluminum oxide (Al_2O_3), iodine vapor (I_2), and oxygen (O_2) [12,17].

Let us focus first on the possible source of aluminum (Al) and aluminum monoxide (AlO). The thermolysis of AIH [12,17] leads to aluminum iodate, which in turn decomposes to aluminum oxide (Al_2O_3), iodine (I_2), and oxygen (O_2). Aluminum oxide (Al_2O_3) has a melting point/decomposition temperature of 2,327 K [28–32]. A maximum temperature of 1,947 K was reached in our experiments for 20 % O_2 (2,190 K for 80 % O_2) implying that the experimental temperature does not exceed the decomposition temperature of aluminum oxide. However, the strong presence of both AlO and Al in the emission spectra indicates that there must be alternate pathways forming Al and AlO prior to the formation of Al_2O_3. It had been previously postulated that metal iodates can form the respective metal monoxide, iodine (I_2), and oxygen (O_2) at temperatures between 673 and 873 K [13,33]. Knowing that the experimental temperatures reach beyond 873 K, it can be predicted that aluminum monoxide (AlO) can form from the decomposition of aluminum iodate via Eq. (1).

$$2\,Al(IO_3)_3 \rightarrow 2\,AlO\left(X^2\Sigma^+\right) + 3\,I_2\left(X^1\Sigma_g^+\right) + 8\,O_2\left(X^3\Sigma_g^-\right) \quad \Delta H_{298} = 3,625\,kJ\,mol^{-1} \tag{1}$$

There is a second potential pathway for the decomposition of aluminum iodate to form aluminum (Al), iodine (I_2), and oxygen (O_2) via Eq. (2). Previous crossed molecular beam experiments showed that atomic aluminum (Al) can react with molecular oxygen to form aluminum monoxide (AlO) plus atomic oxygen (O) via Eq. (3) [34].

$$2\,Al(IO_3)_3 \rightarrow 2\,Al\left(^2P\right) + 3\,I_2\left(X^1\Sigma_g^+\right) + 9\,O_2\left(X^3\Sigma_g^-\right) \quad \Delta H_{298} = 4,151\,kJ\,mol^{-1} \tag{2}$$

$$Al\left(^2P\right) + O_2\left(X^3\Sigma_g^-\right) \rightarrow AlO\left(X^2\Sigma^+\right) + O\left(^3P\right)\Delta H_{298} = -13\,kJmol^{-1} \tag{3}$$

while aluminum monoxide (AlO) can be produced in principle through both pathways ((1) and (3)), the identification of Al emission peaks indicates that not all Al reacts to form AlO. Both pathways are thus open during the combustion of AIH, however energetically reaction (1) is likely the more favorable mechanism. The production of atomic oxygen via Eq. (3) can prove to be vital for the production of other key transients such as iodine monoxide, atomic iodine, and the hydroxyl radical.

Let us consider now the iodine-based products next (I, IO, I_2). Molecular iodine (I_2) is formed in the third step of the AIH decomposition process [16]. Additionally, as discussed above, molecular iodine can form through equations (1) and (2). Oxidation of molecular iodine by atomic oxygen can lead to iodine monoxide (IO) via Eq. (4) [35,36]. This exothermic process can populate the electronic level (A $^2\Pi_{3/2}$) observed spectroscopically via UV–Vis.

$$O\left(^3P\right) + I_2\left(X^1\Sigma_g^+\right) \rightarrow IO\left(X^2\Pi_{3/2}\right) + I\left(^2P\right)\Delta H_{298} = -98\,kJmol^{-1} \tag{4}$$

Finally, water is lost during the first step of the decomposition of AIH, and its emission features are identified in the UV–Vis emission traces. There are two possible reactions forming the hydroxyl radical (OH). Atomic oxygen can initiate an energetically favorable route via abstraction of atomic hydrogen forming the hydroxyl radical (OH) via Eq. (5) [37]. Recall that the assignments of the hydroxyl radical (OH) were also confirmed through the detection of the D1-hydroxyl radical (OD); this in turn suggests reaction (6) as its source.

$$O\left(^3P\right) + H_2O \rightarrow 2\,OH\left(X^2\Pi\right)\Delta H_{298} = 71\,kJmol^{-1} \tag{5}$$

$$O\left(^3P\right) + D_2O \rightarrow 2\,OD\left(X^2\Pi\right)\Delta H_{298} = 73\,kJmol^{-1} \tag{6}$$

The second potential pathway is the homolytic cleavage yielding hydroxyl radicals (OH) and atomic hydrogen (H). This reaction however seems to be less favorable as compared to reaction (5) considering the high bond dissociation energy of 498 kJ mol^{-1} [38,39].

5. Conclusion

In conclusion, the ignition of a single, levitated AIH particle in the presence of O_2 reveals a complex pool of various atoms, radicals, and closed shell species and identifies two distinct stages of ignition. The first ignition stage is the production of a weakly colored orange cloud and the second is the increase in flame brightness followed by a white glow. The first stage is exothermic dissociation of the inner hydrated ring structure with indication of hydroxyl formation. During the second stage, oxidation was confirmed by the appearance of the most intense spectrum with the maximum number of spectral features. The increase in flame brightness during the second stage could be caused by the proposed combustion of released hydrogen from AIH [17,40]. This would provide additional fuel to increase the burn times of AIH and overall increase the efficiency of AIH as an additive for hydrocarbon and solid rocket fuels.

The emission spectra reveal various key transients including atoms, radicals, and closed shell species. First, several atomic emissions were detected, the most important emissions originate from atomic aluminum (Al; ^{2}P) and iodine (I; ^{2}P). In addition to these atomic emissions, atomic oxygen (O; ^{3}P) was also identified at all oxygen concentrations. Secondly, the most prominent emission features are associated with the diatomic radicals, aluminum monoxide (AlO; $X^2\Sigma^+$) and iodine monoxide (IO; $X^2\Pi_{3/2}$). The formation of both diatomic species is exothermic, contributing to the energy generated in the high temperature oxidation reaction. The remaining weak features consist of the hydroxyl radial (OH; X $^2\Pi$). Lastly, two closed shell species have been identified in the emission spectrum, molecular iodine (I_2; $X^1\Sigma_g^+$) and water (H_2O, X^1A_1).

Based on the appearance time and energetics a plausible reaction scheme has been proposed. First is the formation of Al and AlO intermediates along the path from decomposition of $Al(IO_3)_3$ to Al_2O_3.

Since aluminum oxide (Al_2O_3) has a melting point/decomposition temperature of 2,327 K, two alternate pathways were proposed for the formation of Al and AlO. It was predicted based on the work of previous studies [13,33], that both Al and AlO can form from the decomposition of aluminum iodate. The first pathway is the decomposition of aluminum iodate to form aluminum monoxide (AlO), molecular iodine (I_2), and molecular oxygen (O_2). The second pathway is the decomposition of aluminum iodate to form aluminum (Al), molecular iodine (I_2), and molecular oxygen (O_2). Aluminum (Al) can then react with molecular oxygen to form aluminum monoxide (AlO) plus atomic oxygen (O). This primary exothermic step can initiate the course of ignition and has proved to be vital in terms of an instant oxidizer release in the form of reactive atomic oxygen. The production of atomic oxygen is essential for the production of other key transients such as iodine monoxide, atomic iodine, and the hydroxyl radical. Both pathways are predicted to be open during the combustion of AIH, however the first pathway is likely the more favorable mechanism. Additionally, the identification of Al emission peaks indicates that not all Al reacts to form AlO. The formation of AlO is an important finding as AlO is a key transient in the catalytic oxidation of hydrocarbon fuels such as *exo*-tetrahydrodicyclopentadiene (JP-10) [41].

For the iodine containing species (IO, I, I_2), there are two suggested pathways of formation. The first being that I_2 is produced in the third step in the AIH decomposition process [16]. Additionally, as discussed above, molecular iodine is a product of the decomposition of aluminum iodate. I_2 can then react with atomic oxygen, likely formed via equation (3), to form iodine monoxide (IO) and atomic iodine (I). The production of iodine vapor is especially important for the combustion of AIH as it has the potential to enhance the reactivity of aluminum and aid in the overall ignition of AIH [42,43].

Finally, with the water ejected in the first step of the thermal decomposition of AIH, two possible reactions can form the hydroxyl radical (OH). The first being the homolytic cleavage yielding hydroxyl radicals (OH) and atomic hydrogen (H). However, this was unfavorable due to the high bond dissociation energy of 498 kJ mol^{-1} [35,36]. Because of this an alternative reaction can be proposed. This reaction being atomic oxygen initiating the abstraction of atomic hydrogen forming the hydroxyl radical (OH), which serves an oxidizer during combustion processes [44]. Recall that the assignments of the hydroxyl radical (OH) were also confirmed through the detection of the D1-hydroxyl radical (OD); this in turn suggests that OD forms through the abstraction of atomic deuterium by atomic oxygen forming the D1-hydroxyl radical (OD).

Overall, the results represent the understanding of a complex ignition process for an energetic material, i.e., AIH particles in a controlled oxidative medium. By identifying key reaction intermediates and the plausible formation pathways, a predictive combustion model can be prepared when used in an air breathing propulsion system. The knowledge of the reactive species provides an understanding of the gas-phase oxidation of AIH in doped hydrocarbon fuels such as JP-10, ultimately aiding the development of next generation additives for hydrocarbon and solid rocket fuels.

CRediT authorship contribution statement

Grace L. Rizzo: Writing – original draft, Visualization, Methodology, Investigation, Formal analysis, Data curation. **Souvick Biswas:** Writing – review & editing, Visualization, Methodology. **Michelle L. Pantoya:** Writing – review & editing, Validation, Resources. **Ralf I. Kaiser:** Writing – review & editing, Validation, Supervision, Project administration, Funding acquisition.

Declaration of competing interest

The authors declare that they have no known competing financial interests or personal relationships that could have appeared to influence the work reported in this paper.

Data availability

Data will be made available on request.

Acknowledgment

The Hawaii group was supported by the United States Office of Naval Research (ONR) under Contract Number N00014-22-1- 2010. The Texas Tech group is supported for this work by the United States Army Research Office (ARO) under Grant Number W911NF-22-2-0170. Dr. Kelsea Miller and Mr. Joseph Pantoya, both from Texas Tech, are gratefully acknowledged for preparing the AIH particles used in this study.

Appendix A. Supplementary data

Supplementary data to this article can be found online at https://doi.org/10.1016/j.cplett.2024.141212.

References

[1] E. Eckermann, World history of the automobile, Society of Automotive Engineers, Warrendale, PA, 2001.
[2] E.M. Goodger, Hydrocarbons as a source of energy, in: Hydrocarbon Fuels, Palgrave, London, 1975, pp. 3–20.
[3] Y.J. Zhou, E.J. Kerkhoven, J. Nielsen, Barriers and opportunities in bio-based production of hydrocarbons, Nat. Energy 3 (2018) 925–935.
[4] H. Li, J. Qin, W. Bao, H. Huang, Performance improvement of gaseous hydrocarbon fuel driven thermal power generation systems for hypersonic vehicles, Energy Convers. Manag. 199 (2019) 111949.
[5] E.L. Dreizin, Metal-based reactive nanomaterials, Prog. Energy Combust. Sci. 35 (2009) 141–167.
[6] E. Xiu-Tian-Feng, L. Pan, F. Wang, L. Wang, X. Zhang, J.J. Zou, Al-Nanoparticle-containing nanofluid fuel: synthesis, stability, properties, and propulsion performance, Ind. Eng. Chem. Res. 55 (2016) 2738–2745.
[7] M. Lucas, S.J. Brotton, A. Min, M.L. Pantoya, R.I. Kaiser, Oxidation of levitated exo-Tetrahydrodicyclopentadiene droplets doped with aluminum nanoparticles, J. Phys. Chem. Lett. 10 (2019) 5756–5763.
[8] B. Dikici, S.W. Dean, M.L. Pantoya, V.I. Levitas, R.J. Jouet, Influence of aluminum passivation on the reaction mechanism: flame propagation studies, Energy and Fuels 23 (2009) 4231–4235.
[9] J. Gesner, M.L. Pantoya, V.I. Levitas, Effect of oxide shell growth on nano-aluminum thermite propagation rates, Combust. Flame 159 (2012) 3448–3453.
[10] M.A. Trunov, S.M. Umbrajkar, M. Schoenitz, J.T. Mang, E.L. Dreizin, Oxidation and melting of aluminum nanopowders, J. Phys. Chem. B 110 (2006) 13094–13099.
[11] D.K. Smith, D.K. Unruh, C.C. Wu, M.L. Pantoya, Replacing the Al_2O_3 shell on al particles with an oxidizing salt, aluminum iodate hexahydrate. part I: reactivity, J. Phys. Chem. C 121 (2017) 23184–23191.
[12] J. Kalman, D.K. Smith, K.K. Miller, S.K. Bhattacharia, K.R. Bratton, M.L. Pantoya, A strategy for increasing the energy release rate of aluminum by replacing the alumina passivation shell with aluminum iodate hexahydrate (AIH), Combust. Flame 205 (2019) 327–335.
[13] I. Shancita, K.K. Miller, P.D. Silverstein, J. Kalman, M.L. Pantoya, Synthesis of metal iodates from an energetic salt, RSC Adv. 10 (2020) 14403–14409.
[14] I. Shancita, L.L. Campbell, C.C. Wu, A.J.A. Aquino, S.D. Walck, D. Tunega, M. L. Pantoya, Effect of hydration on promoting oxidative reactions with aluminum oxide and oxyhydroxide nanoparticles, J. Phys. Chem. C 123 (2019) 15017–15026.
[15] D.K. Smith, M.N. Bello, D.K. Unruh, M.L. Pantoya, Synthesis and reactive Characterization of aluminum iodate hexahydrate crystals $[Al(H_2O)_6](IO_3)_3(HIO_3)_2$, Combust. Flame 179 (2017) 154–156.
[16] G.L. Rizzo, S. Biswas, I. Antonov, K.K. Miller, M.L. Pantoya, R.I. Kaiser, Exotic inverse kinetic isotopic effect in the thermal decomposition of levitated aluminum iodate hexahydrate particles, J. Phys. Chem. Lett. 14 (2023) 2722–2730.
[17] K.K. Miller, S.E. Creegan, D.K. Unruh, J.D. Pantoya, K.J. Hill, Q. Tran, M. L. Pantoya, Acid-base synthesis of aluminum iodate hexahydrate powder as a promising propellant oxidizer, Chem. Eng. J. 453 (2023) 139953.
[18] S.J. Brotton, R.I. Kaiser, Novel high-temperature and pressure-compatible ultrasonic levitator apparatus coupled to raman and fourier transform Infrared spectrometers, Rev. Sci. Instrum. 84 (2013) 055114.
[19] S.J. Brotton, R.I. Kaiser, In situ raman spectroscopic study of gypsum ($CaSO_4 \cdot 2H_2O$) and epsomite ($MgSO_4 \cdot 7H_2O$) dehydration utilizing an ultrasonic levitator, J. Phys. Chem. Lett. 4 (2013) 669–673.
[20] S. Biswas, I. Antonov, K. Fujioka, G.L. Rizzo, S.D. Chambreau, S. Schneider, R. Sun, R.I. Kaiser, Unraveling the initial steps of the ignition chemistry of the hypergolic ionic liquid 1-Ethyl-3-methylimidazolium cyanoborohydride ([EMIM][CBH]) with nitric acid (HNO3) exploiting chirped pulse triggered droplet merging, Phys. Chem. Chem. Phys. 25 (2023) 6602–6625.

[21] M. Lucas, S.J. Brotton, A. Min, C. Woodruff, M.L. Pantoya, R.I. Kaiser, Effects of size and prestressing of aluminum particles on the oxidation of levitated exo-Tetrahydrodicyclopentadiene droplets, J. Phys. Chem. A 124 (2020) 1489–1507.
[22] I. Antonov, A. Chyba, S.D. Perera, A.M. Turner, M.L. Pantoya, M.T. Finn, A. Epshteyn, R.I. Kaiser, Discovery of discrete stages in the oxidation of exo-Tetrahydrodicyclopentadiene ($C_{10}H_{16}$) droplets doped with titanium-aluminum-boron reactive mixed-metal nanopowder, J. Phys. Chem. Lett. 13 (2022) 9777–9785.
[23] Y. Ralchenko, A. Kramida, J. Reader, NIST: Atomic Spectra Database Lines https://physics.nist.gov/PhysRefData/ASD/lines_form.html (accessed Oct 18, 2023).
[24] PGOPHER https://pgopher.chm.bris.ac.uk/ (accessed Oct 18, 2023).
[25] S.M. Newman, W.H. Howie, I.C. Lane, M.R. Upson, A.J. Orr-Ewing, Predissociation of the a $^2\Pi_{3/2}$ state of IO studied by cavity ring-down spectroscopy, J. Chem. Soc. Faraday Trans. 94 (1998) 2681–2688.
[26] P. Spietz, J.C. Gómez Martín, J.P. Burrows, Spectroscopic studies of the I_2/O_3 photochemistry: Part 2. improved spectra of iodine oxides and analysis of the IO absorption Spectrum, J. Photochem. Photobiol. A Chem. 176 (2005) 50–67.
[27] A.K. Shuaibov, A.I. Minya, Z.T. Gomoki, R.V. Gritsak, Optical Characteristics of an electric-Discharge source of ultraviolet radiation based on a mixture of argon with heavy water (D_2O) vapor, Opt. Spectrosc. (english Transl. Opt. i Spektrosk. 114 (2013) 193–196.
[28] B. Bhushan, B.K. Gupta, Handbook of Tribology : materials, coatings, and Surface treatments, McGraw-Hill, New York, NY, 1991.
[29] A.N. Samant, N.B. Dahotre, Computational predictions in single-dimensional laser machining of alumina, Int. J. Mach. Tools Manuf. 48 (2008) 1345–1353.
[30] R. Friedman, A. Maček, Ignition and combustion of aluminium particles in hot ambient gases, Combust. Flame 6 (1962) 9–19.
[31] R. Friedman, A. Maček, Combustion studies of single aluminum Particles, Symp. Combust. 9 (1963) 703–712.
[32] S.K. Bhaumik, C. Divakar, S. Usha Devi, A.K. Singh, Synthesis and sintering of SiC under high pressure and high temperature, J. Mater. Res. 14 (1999) 906–911.
[33] H. Wang, D.J. Kline, M. Rehwoldt, M.R. Zachariah, Ignition and combustion Characterization of $Ca(IO_3)_2$-based pyrotechnic composites with B, Al, and Ti, Propellants, Explos. Pyrotech. 43 (2018) 977–985.
[34] M. Saba, T. Kato, T. Oguchi, Reaction modeling study on the combustion of aluminum in gas phase: the Al + O_2 and related reactions, Combust. Flame 225 (2021) 535–550.
[35] D. Hölscher, C. Fockenberg, R. Zellner, LIF detection of the IO-radical and Kinetics of the reactions $I+O_3 \rightarrow IO+O_2$, $O(^3P)+I_2 \rightarrow IO+I$, $O(^3P)+CH_3I \rightarrow IO+CH_3$ and $O(^3P)+CF_3I \rightarrow IO+CF_3$ in the temperature range 230 to 310 K, Berichte Der Bunsengesellschaft Für Phys. Chemie 102 (1998) 716–722.
[36] H.W. Chang, G. Burns, Recombination of iodine atoms by flash photolysis over a wide temperature range. VII. recombination between 206 and 300 °K, J. Chem. Phys. 64 (1976) 349–353.
[37] P. Politzer, P. Lane, M. Edward Grice, Energetics of aluminum combustion, J. Phys. Chem. A 105 (2001) 7473–7480.
[38] J.A. Dean, Bond dissociation energies, in: Lange's Handbook of Chemistry, McGraw-Hill, InC, New York, NY, 1999, pp. 41–53.
[39] B. Darwent, Bond dissociation energies in simple molecules, National Bureau of Standards, Washington, 1970.
[40] C.J. Miller, E.R. Wainwright, J.L. Gottfried, J. Abraham, L. Wei, M.L. Pantoya, The influence of particle size on the fluid dynamics of a laser-induced plasma, Phys. Fluids 34 (2022) 53312.
[41] S. Biswas, D. Paul, C. He, N. Dias, M. Ahmed, M.L. Pantoya, R.I. Kaiser, Counterintuitive catalytic reactivity of the aluminum oxide "passivation" Shell of aluminum Nanoparticles facilitating the thermal decomposition of exo-Tetrahydrodicyclopentadiene (JP-10), J. Phys. Chem. Lett. 14 (2023) 9341–9350.
[42] S. Zhang, C. Badiola, M. Schoenitz, E.L. Dreizin, Oxidation, ignition, and combustion of Al·I_2 composite powders, Combust. Flame 159 (2012) 1980–1986.
[43] B.K. Little, E.J. Welle, S.B. Emery, M.B. Bogle, V.L. Ashley, A.M. Schrand, C. M. Lindsay, Chemical dynamics of Nano-aluminum/iodine (V) oxide, J. Phys. Conf. Ser. 500 (2014) 052025.
[44] S.J. Brotton, R.I. Kaiser, Effects of nitrogen dioxide on the oxidation of levitated exo-Tetrahydrodicyclopentadiene (JP-10) droplets doped with aluminum nanoparticles, J. Phys. Chem. A 125 (2021) 2727–2742.